

High-resolution ALMA observations of V4046 Sgr: a circumbinary disc with a thin ring

Rafael Martinez-Brunner,¹★ Simon Casassus,¹ Sebastián Pérez,² Antonio Hales,³ Philipp Weber,^{1,2}

Carla Arce-Tord, Lucas Cieza, Antonio Garufi, Sebastián Marino, Alice Zurlo

¹*Departamento de Astronomía, Universidad de Chile, Casilla 36-D, Santiago, Chile*

²*Universidad de Santiago de Chile, Av. Ecuador 3659, Santiago*

Accepted XXX. Received YYY; in original form ZZZ

ABSTRACT

The nearby V4046 Sgr spectroscopic binary hosts a gas-rich disc known for its wide cavity and dusty ring. We present high resolution (~ 20 – 50 mas) ALMA observations of the 1.3 mm continuum which, combined with SPHERE-IRDIS polarized images and a well-sampled spectral energy distribution (SED), allow us to propose a physical model for the source using radiative transfer (RT) predictions. The new ALMA data reveal a very thin ring at a radius of 13.15 ± 0.26 au (Ring13), with a marginally resolved radial width of 2.46 ± 0.56 au. Ring13 is surrounded by a ~ 10 au-wide gap, and it is flanked by a very mm-bright outer ring (Ring24) with a sharp inner edge at 24 au. The steeply decreasing brightness of Ring24 breaks at ~ 35 au into a shallow tail. In order to reproduce the SED, the model that we propose requires an inner ring at ~ 5 au (Ring5) composed mainly of small dust grains, hiding under the IRDIS coronagraph, and surrounding an inner circumbinary disc. The surprisingly thin Ring13 is nonetheless roughly 4 times wider than the model scale height, and could thus be long-lived. The strong near-far disc asymmetry at $1.65 \mu\text{m}$ points at a very forward-scattering phase function, and requires grain radii of no less than $0.4 \mu\text{m}$. The previously reported scattered-light shadow of the secondary star is also reproduced by the RADMC3D RT package.

Key words: protoplanetary discs – submillimetre: planetary systems – radiative transfer

1 INTRODUCTION

Recent observations of young circumstellar discs have transformed current knowledge of planet formation. The focus of resolved imaging with the Atacama Large Millimetre/submillimetre Array (ALMA) or with the current generation of high-contrast cameras has mainly been towards the brighter sources (e.g. Andrews 2020). It is to address this bias that the programme called “Discs Around T Tauri Stars with SPHERE” (DARTTS-S) collected differential polarization imaging (DPI) data secured with the Spectro-Polarimeter High-contrast Exoplanet REsearch (SPHERE Beuzit et al. 2019) in a total of 29 solar-type stars (Avenhaus et al. 2018; Garufi et al. 2020). The sample is not biased towards exceptionally bright and large discs. The DARTTS observations revealed diverse structures and morphologies in the scattering surface of these discs. This letter on V4046 Sagittarii (Sgr) is part of a companion programme, the DARTTS survey with ALMA (DARTTS-A, Perez et al. *in prep*), which will present millimetre observations of nine protoplanetary discs previously imaged in polarized scattered light in DARTTS-S.

V4046 Sgr is a double-lined spectroscopic binary of K-type stars (K5 and K7) with very similar masses of $0.90 \pm 0.05 M_{\odot}$ and $0.85 \pm 0.04 M_{\odot}$ (Rosenfeld et al. 2012), on a close ($a \approx 0.041$ au), circular ($e \leq 0.01$) orbit, with an orbital period of 2.42 days (Quast et al. 2000). It is a member of the β Pictoris moving group (Zucker-

man & Song 2004), with an estimated age of 23 ± 3 Myr (Mamajek & Bell 2014), and its distance is 71.48 ± 0.11 pc (Collaboration et al. 2020). V4046 Sgr hosts a massive ($\sim 0.1 M_{\odot}$) circumbinary disc extending to ~ 300 au (Rosenfeld et al. 2013; Rodríguez et al. 2010), rich in diverse molecular lines (Kastner et al. 2018).

The observations, including new 1.3 mm continuum data, are described in Section 2. We interpret the data in terms of a parametric model, presented in Section 3, which builds up on the previous models of V4046 Sgr (Rosenfeld et al. 2013; Ruíz-Rodríguez et al. 2019; Qi et al. 2019) to account for the new ALMA data. Our results are discussed in Section 4 and summarised in Section 5.

2 OBSERVATIONS

New ALMA observations of V4046 Sgr were obtained in 2017 as part of the Cycle 5 program 2017.1.01167.S (PI: S. Perez). The observations acquired simultaneously the 1.3 mm continuum and the $J = 2-1$ line of ^{12}CO with (i.e. with a band 6 211–275 GHz correlator setup). The ALMA array was in its C43-8 configuration, with baselines ranging from 92 to 8548 m which translate into a synthesized beam of $0''.062 \times 0''.055$, in natural weights. Here we focus on the continuum observations only.

V4046 Sgr was observed in differential polarization imaging (DPI) mode with SPHERE-IRDIS on March 13, 2016 (see Avenhaus et al. 2018, for details). Here we use a new reduction of the H band data produced with the IRDAP pipeline (van Holstein et al. 2020), which

★ E-mail: rmartinezbrunner@gmail.com

can separate stellar and instrumental polarization. The polarized signal is consistent with the previous image in [Avenhaus et al. \(2018\)](#). The degree of linear polarization of the central and unresolved signal in V4046 Sgr is only 0.13%, with a systematic uncertainty of 0.05% due to time-varying atmospheric conditions during the exposures. The angle of polarization is aligned with the disc major axis, as expected given that the target has $A_V=0.0$ ([McJunkin et al. 2016](#)) and the entire polarization is dominated by circumstellar rather than inter-stellar material.

Image synthesis of the ALMA continuum was performed with the *uvmem* package ([Casassus et al. 2006](#); [Cárcamo et al. 2018](#)), which fits a non-parametric model image I_j^m to the data by comparing the observed and model visibilities, V_k^o and V_k^m , using a least-squares figure of merit L :

$$L = \sum_{k=1}^N \omega_k |V_k^o - V_k^m|^2 + \lambda S. \quad (1)$$

The regularization term S depends on the application, and in this case we chose the standard image entropy, or

$$S = \sum_{j=1}^M \frac{I_j^m}{M} \ln \left(\frac{I_j^m}{M} \right), \quad (2)$$

where M is the default pixel intensity value, and is set to 10^{-3} times the theoretical noise of the dirty map (as inferred from the visibility weights ω_k). Here we set $\lambda = 0.01$. Similar applications of *uvmem* in the context of protoplanetary discs can be found, for example, in [Casassus et al. \(2013, 2018, 2019a\)](#); [Pérez et al. \(2019\)](#). An advantage of *uvmem* compared to more traditional imaging strategies, such as provided by the *tclean* task in CASA, is that the effective angular resolution of the model image is ~ 3 times finer than the natural weights clean beam ([Cárcamo et al. 2018](#)). This angular resolution is comparable to uniform or super-uniform weights in *tclean*, but it preserves the natural-weights point-source sensitivity.

The resulting *uvmem* image shown in the top right panel of Fig. 1 exhibits previously unseen substructure of the disc. This image reveals that the disc features two rings of large dust grains with a broad gap between them, i.e. Ring13 at 13 au and Ring24 starting at 24 au. The wide and bright Ring24 reaches its peak intensity at ~ 30 au, beyond which it drops steeply before breaking at ~ 35 au into a shallow tail. While this is the first observation of Ring13, [Ruíz-Rodríguez et al. \(2019\)](#) did anticipate its existence as their ALMA continuum image showed a distinct excess between ~ 10 and 17 au.

Ring13 is surprisingly narrow and seems to be off-centred relative to the GAIA stellar position, at the origin of coordinates in Fig. 1. We determined the ring's centre and orientation by minimising the dispersion of the disc radial profiles from 6 au to 19 au, by using the *MPolarMaps* package described in [Casassus et al. \(2021, in prep\)](#). The resulting disc orientation is set at a position angle (PA) of $77.31 \pm 0.03^\circ$, with an inclination of $32.96 \pm 0.02^\circ$, and the optimal ring centre is at $\Delta\alpha = -4 \pm 0.02$ mas $\Delta\delta = 13 \pm 0.05$ mas relative to the GAIA position of the stars. The offset of the center of the cavity and the nominal stellar positions is entirely consistent with a pointing error, since the pointing accuracy of ALMA is usually taken to be 1/10 of the natural-weights beam, at 1σ , or ~ 6 mas in this case. ***ANTONIO PLEASE CONFIRM AND PROVIDE A REFERENCE***

The ring width can be measured in polar coordinates by fitting 1-D Gaussians, thus obtaining a width and centroid at each azimuth. On average, we obtained a FWHM of 2.83 ± 0.50 au, and a stellocentric radius of 13.15 ± 0.26 au (See Fig. 2). As the *uvmem* model image has

an effective angular resolution of $\sim 1/3$ that of the natural-weighted beam ($0''.062 \times 0''.055$), we see that Ring13 is marginally resolved. After subtraction of the approximate *uvmem* resolution ($\sim 0''.021 \times \sim 0''.018$), the ring width is $\sim 2.46 \pm 0.56$ au.

In a second optimization of the disc orientation, but this time aiming for Ring24 with a radial domain from 20 au to 70 au, we obtained a PA of $76.86 \pm 0.02^\circ$, with an inclination of $33.92 \pm 0.01^\circ$ and a centre at $\Delta\alpha = 2 \pm 0.02$ mas $\Delta\delta = 12 \pm 0.02$ mas relative to the stars. We see that both Ring13 and Ring24 both share a very similar orientation and centre, given the errors. However, perhaps due to the joint effect of all these small differences, we can see that there are some hints for a somewhat different orientation, as summarised in Fig. 2.

Interestingly, the ALMA image also detects faint 1.3 mm continuum emission near the stellar positions (See the inset in Fig. 1). Since this faint central emission is larger than the angular resolution, it is probably stemming from thermal emission from large dust grains rather directly from the stars. The main blob of this dust structure is at a estimate distance of only $0''.012 \pm 0''.002$, or $\sim 0.85 \pm 0.14$ au from the binary system, and, estimating its form as a Gaussian ellipse, it has a FWHM of ~ 1.43 au. If this feature is caused by the presence of millimeter-size dust, its estimated mass would be around $0.12 M_\oplus$.

The scattered-light image in the top left panel of Fig. 1 also shows a double ring structure in the micron-sized dust distribution. The observed morphology presents an inner cavity of ~ 10 au in radius and two rings located at 14.10 ± 0.01 , coincident with Ring13, and 24.62 ± 0.08 au, coincident with Ring24, with a small gap between them at ~ 20 au. The observed second ring matches the inner wall of the 1.3 mm continuum emission outer ring ([Ruíz-Rodríguez et al. 2019](#)). Two other important features that are present in the image are: the brightness asymmetry, and the shadows projected on the disc by the close binary system as they eclipse each other, discovered by [D'Orazi et al. \(2019\)](#).

The binary phase reported by [D'Orazi et al. \(2019\)](#) in the scattered-light observation is at a position angle (PA) of 265° , east of north. Using this measurement, the binary phase was calculated at the time of the ALMA observation at a PA of $\sim 80^\circ$. There is no hint of radio decrements in either Rings13 nor in Ring24 that would match shadowing at this PA. This could be explained by inefficient disc cooling compared to the speed of the illumination pattern (see [Casassus et al. 2019b](#), for estimates of this cooling timescale).

The observed SED was collected from data in the literature ([Helou & Walker 1988](#); [Hutchinson et al. 1990](#); [Jensen & Mathieu 1997](#); [Høg et al. 2000](#); [Kharchenko 2001](#); [Cutri et al. 2003](#); [Murakami et al. 2007](#); [Ofek 2008](#); [Ishihara et al. 2010](#); [Cutri & et al. 2012](#)), available online in *VIZIER*. We also used archival *Spitzer* IRS spectroscopic data (see Fig. 3).

3 PARAMETRIC RADIATIVE TRANSFER MODEL

The multi-frequency data can be interpreted in terms of a physical structure using radiative transfer predictions, for which we used the *RADMC3D* package ([Dullemond et al. 2012](#)). The general framework of the parametric model that we used is similar to that in [Casassus et al. \(2018\)](#) for DoAr 44, and the initial model values were inspired from those in [Rosenfeld et al. \(2013\)](#). Through trial and error, we found a set of values for the parameters that correctly fit the available data. The final structure of the parametric model is summarised in Fig. 4.

The stars were modeled using two Kurucz photospheres models ([Kurucz 1979](#); [Castelli et al. 1997](#)), with $T_{\text{eff},1} = 4350$ K,

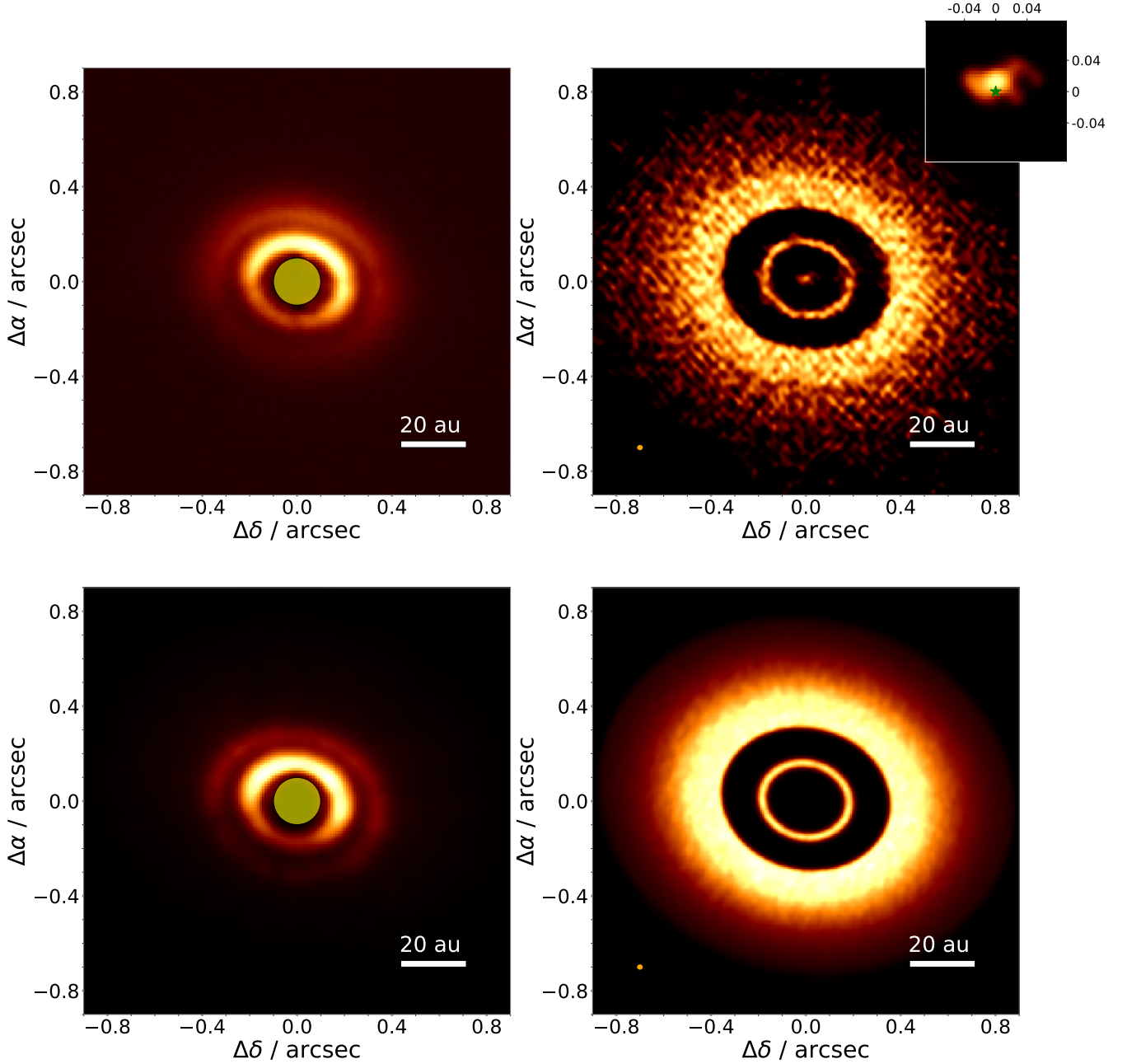


Figure 1. Comparison of observations (top) and simulated images (bottom) at $1.65\ \mu\text{m}$ (left) and $1.3\ \text{mm}$ continuum (right) of the circumbinary disc orbiting V4046 Sgr. *Top left panel:* SPHERE-IRDIS H -band image with a yellow filled circle that represents the N_ALC_YJH_S coronagraph with a radius of $\sim 0''.12$, or $\sim 8.6\ \text{au}$ at $71.48\ \text{pc}$. *Top right panel:* $1.3\ \text{mm}$ continuum uvmem model image. The small orange ellipse shows an estimated uvmem beam size ($\sim 0''.021 \times \sim 0''.018$). The inset zooms into the central emission, and the green star marks the binary position. *Bottom left panel:* synthetic image at $1.65\ \mu\text{m}$. *Bottom right panel:* synthetic image at $1.3\ \text{mm}$. For all the images in the figure the colour scale is linear.

$R_{*,1} = 1.064 R_{\odot}$, $M_{*,1} = 0.90 M_{\odot}$ and $T_{\text{eff},2} = 4060\ \text{K}$, $R_{*,2} = 1.033 R_{\odot}$, $M_{*,2} = 0.85 M_{\odot}$ respectively and with an accretion rate of $\log(\dot{M}/(M_{\odot}\ \text{yr}^{-1})) = -9.3$ for both cases to include excess UV due to stellar accretion (Donati et al. 2011). The stars were placed at a mutual separation of $0.041\ \text{au}$, so that their centre of mass coincides with the origin, and oriented at a PA of 250° , so that the secondary

lies to the NWW from the primary, thus casting the same shadow as observed by D’Orazi et al. (2019).

Reproducing the radial and vertical structure of the V4046 Sgr disc turned out to be challenging. We built the model in terms of the gas distribution, and with two different dust populations: larger grains that are vertically settled and dominate the total dust mass,

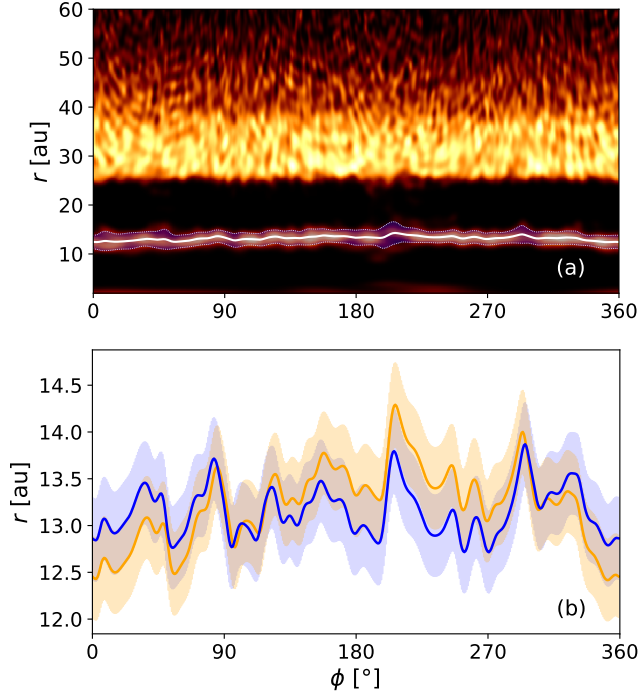


Figure 2. (a) Polar decomposition of the 1.3 mm continuum image, using the orientation of Ring24. We trace Ring13 using the centroids (solid line) and width of radial Gaussian fits (blue region between the dotted lines). (b) Centroid of Ring13, for two disc orientations: the orange line corresponds to the same trace as in a), while the blue line is obtained for the inner ring orientation.

and a population of smaller grains that are uniformly mixed with the gas and reach higher regions above the mid-plane.

Assuming a three dimensional model in a cylindrical reference frame with coordinates (r, θ, z) , the gas density (ρ_{gas}) distribution follows

$$\rho_{\text{gas}}(r, z) = \frac{\Sigma_{\text{gas}}(r)}{\sqrt{2\pi} H(r)} \exp \left[-\frac{1}{2} \left(\frac{z}{H(r)} \right)^2 \right], \quad (3)$$

where $H(r)$ is the scale height profile and $\Sigma_{\text{gas}}(r)$ is the gas surface density profile.

The parametric scale height profiles for the gas and for each dust population are

$$H(r) = \chi H_0 [r/r_0]^{\psi(r)}, \quad (4)$$

where H_0 is the scale height at $r = r_0$, ψ is the flaring index and χ is a scaling factor (in the range 0 – 1) that mimics dust settling. The gas and the small dust (sd) grains have no settling, so $\chi_{\text{gas}} = \chi_{\text{sd}} = 1$. The radial spread of Ring13 appears two to three times wider in the gas-tracing NIR observations than in the fluxes received from larger grains with ALMA. We assume that the same ratio holds in the vertical direction (due to the settling of larger grains towards the disc's midplane), leading to $\chi_{\text{ld}} = 0.4$.

For the vertical structure, D'Orazi et al. (2019) found flaring angles of $\varphi = 6.2 \pm 0.6^\circ$ for the inner ring and $\varphi = 8.5 \pm 1.0^\circ$ for the outer one. Our model uses the same values, with two different flaring indices, ψ_1 and ψ_2 . The separation between the two values were set at $r = 18$ au with $\psi_1 = 0.2$ for Ring5 and Ring13, and $\psi_2 = 0.5$ for Ring24. The scale height is $H_0 = 0.88$ au at $r_0 = 18$ au.

We propose a three ringed structure to reproduce the observations.

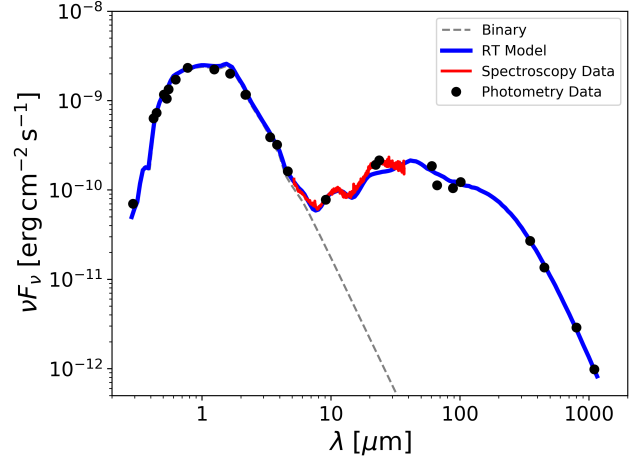


Figure 3. The observed SED of V4046 Sgr (black points and solid red curve) compared with the model (blue). The black points represent the measured photometry and the red line shows an archival *Spitzer* IRS spectrum. The dashed silver curve shows the emission of the stellar photosphere model.

We separate the disc into four individual regions: the inner disc, Ring5, Ring13 and Ring24. The combined gas surface density profile is then given by:

$$\Sigma_{\text{gas}}(r) = \Sigma_{\text{inner disc}} + \Sigma_{\text{Ring5}} + \Sigma_{\text{Ring13}} + \Sigma_{\text{Ring24}} \quad (5)$$

The inner disc follows a power law function defined by

$$\Sigma_{\text{inner disc}}(r) = \Sigma_c \left(\frac{r}{R_c} \right)^{-\gamma} \exp \left[-\left(\frac{r}{R_c} \right)^{2-\gamma} \right], \quad (6)$$

where R_c is a characteristic radius and γ is the surface density power-law index. We used $R_c = 16$ au, $\Sigma_c = 3.26 \times 10^{-4} \text{ g cm}^{-3}$ and a fixed $\gamma = 1$ as it is a typical value for discs (Andrews et al. 2009, 2010). Our model extends from 0.3 au outwards, as the interior is expected to be cleared by dynamical effects of the central binary (Artymowicz & Lubow 1994).

We choose to use Gaussian profiles to parameterize Ring5 and Ring13,

$$\Sigma_{\text{ring}}(r) = \frac{\Sigma_o}{\sqrt{2\pi}\sigma} \exp \left[-\frac{1}{2} \left(\frac{r - \mu}{\sigma} \right)^2 \right], \quad (7)$$

where we define constants that correspond to the centroid radii $\{\mu_{\text{Ring5}} = 5.5 \text{ au}, \mu_{\text{Ring13}} = 14.9 \text{ au}\}$, ring widths $\{\sigma_{\text{Ring5}} = 1 \text{ au}, \sigma_{\text{Ring13}} = 2.3 \text{ au}\}$, and normalizations $\{\Sigma_{o,\text{Ring5}} = 3.28 \text{ au g cm}^{-3}, \Sigma_{o,\text{Ring13}} = 6 \times 10^{-1} \text{ au g cm}^{-3}\}$ for both components separately.

For Ring24 we used the same power law as for the inner disc but scaled by an empirically obtained factor, $\delta_{\text{sd}} = 4.2 \times 10^4$:

$$\Sigma_{\text{Ring24}}(r) = \Sigma_{\text{inner disc}}(r) \delta_{\text{sd}}, \quad (8)$$

The inner edge of Ring24 follows a different profile. Between R_{in} and R_{peak} , which respectively mark the inner edge and the location of maximum density of the outer ring, the gas density profile is multiplied by an additional factor

$$\epsilon(r) = \left(\frac{r - R_{\text{in}}}{R_{\text{peak}} - R_{\text{in}}} \right)^3. \quad (9)$$

This parameter allows us to model a smoother inner edge of the outer ring, with $R_{\text{in,gas}} = 18.0$ au and $R_{\text{peak,gas}} = 26.4$ au. This factor is

also applied to the large dust population with $R_{\text{in,ld}} = 24.2$ au and $R_{\text{peak,ld}} = R_{\text{peak,gas}}$.

The total dust-to-gas mass ratio is taken to be $\zeta = 0.047$ (as in Rosenfeld et al. 2013). The small dust grains are assumed to only make up for a fraction of $f_{\text{sd}} = 1\%$ of the total dust mass. As small dust is typically tightly coupled to the gas dynamics, its density profile is expected to follow the gas density. Then the density of small dust can be calculated as:

$$\rho_{\text{small-dust}}(r, z) = \rho_{\text{gas}}(r, z) f_{\text{sd}} \zeta. \quad (10)$$

Since the large dust grains are less coupled to the gas, their distribution has some important differences that require a special parameterisation, with a larger inner cavity, a larger gap between Ring13 and Ring24, and a break in the outer ring. To be consistent with the theory, Ring5 should have a small large-dust population too, but, as this ring is not visible in the ALMA observation, we added just the right mass to be undetectable by the ALMA observation. We also truncated the profile of large dust grains at 63 au. It is then defined by the sum of its three components

$$\Sigma_{\text{ld}}(r) = \Sigma_{\text{Ring5,ld}} + \Sigma_{\text{Ring13,ld}} + \Sigma_{\text{Ring24,ld}}. \quad (11)$$

For Ring5 and Ring13, we choose Gaussian profiles parameterized with centroid radii $\mu_{\text{Ring5,ld}} = 5.5$ au and $\mu_{\text{Ring13,ld}} = 13.22$ au, ring widths of $\sigma_{\text{Ring5,ld}} = 0.4$ au and $\sigma_{\text{Ring13,ld}} = 0.85$ au, and normalizations $\Sigma_{\text{o,Ring5,ld}} = 1.34 \times 10^{-4}$ au g cm $^{-3}$ and $\Sigma_{\text{o,Ring13,ld}} = 2.41$ au g cm $^{-3}$. For Ring24 we used the same profile as for the gas, but with the difference that, in an effort to recreate the break seen in the outer ring, we choose different values for $\gamma = -3.5$ and $R_c = 39$ au between 27.9 and 35.3 au. The surface density for large dust grains in the outer ring is thus given by

$$\Sigma_{\text{Ring24,ld}}(r) = \Sigma_c \left(\frac{r}{R_c} \right)^{-\gamma} \exp \left[- \left(\frac{r}{R_c} \right)^{2-\gamma} \right] \delta_{\text{ld}}(r), \quad (12)$$

where

$$\delta_{\text{ld}}(r) = \begin{cases} 0 & r < 24.6 \text{ au} \\ 7.19 \times 10^4 & 24.6 < r < 27.9 \text{ au} \\ 3.17 \times 10^4 & 27.9 < r < 35.3 \text{ au} \\ 2.65 \times 10^5 & 35.3 < r < 64 \text{ au}. \end{cases} \quad (13)$$

Then the final density of large dust can be calculated as

$$\rho_{\text{large dust}}(r, z) = \frac{\Sigma_{\text{ld}}(r)}{\sqrt{2\pi} H(r)} \exp \left[- \frac{1}{2} \left(\frac{z}{H(r)} \right)^2 \right] f_{\text{ld}} \zeta. \quad (14)$$

The two different populations of dust grains correspond to small grains, with radii ranging from 0.3 to 1.5 μm , and large dust grains, with radii from 0.3 μm to 10 mm. We computed the dust opacities using the `bhmi` code provided in the `RADMC3D` package, with a mix composed of 60% silicate, 20% graphite and 20% ice.

The observed near-far asymmetry in the DPI image is suggestive of a strongly forward-scattering phase function. In order to reproduce a similar asymmetry, we used much larger grains than typically used in the RT modelling of such near-IR data (e.g., Casassus et al. 2018).

The simulated DPI image at 1.65 μm in Fig. 1 was obtained with the scattering matrix calculated by the `makeopac.py` script provided in the `RADMC3D` package. As a way of reproducing the H -band image, we used a different grain size distribution, where we centred a Gaussian at 0.4 μm , smeared out by 30%, and with distributed over 20 bins within that range. This distribution applies only to generate the NIR Q_ϕ image. To produce this Q_ϕ image we performed a linear combination of the two orthogonal linear polarizations U and Q ,

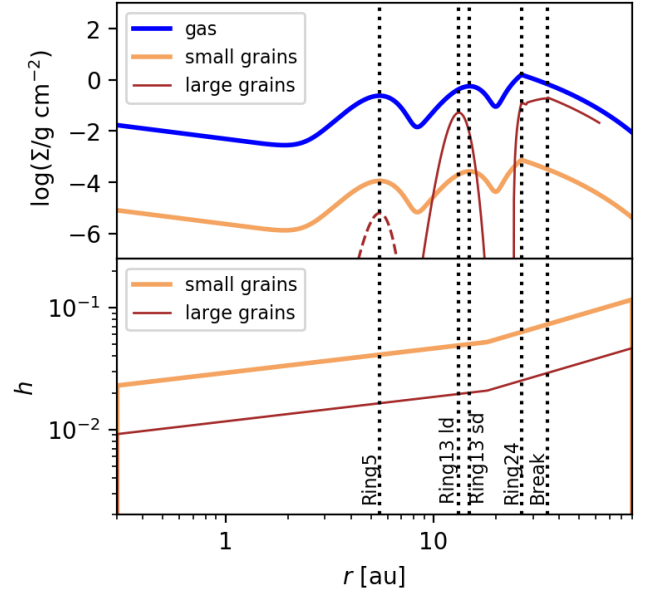


Figure 4. **Top:** surface density profiles for gas, large and small dust grains. **Bottom:** Aspect ratio profile $h(r) = H(r)/r$. The dashed brown line indicates the undetectable large grains in Ring5. The dotted lines crossing both panels correspond to transition radii in the parametric model.

following Avenhaus et al. (2017), which gives a representation of an unbiased estimate of the polarized intensity image.

The inner radius of the model grid was set to 0.1 au, and the outer radius to 100 au, which is large enough for the dust disc to be undetectable. We set the values of the inclination and disc position angle to the same as obtained from the ALMA observation in Section 2, such that the model has an inclination of $i = 32.96^\circ$ and a P.A. = 77.31° . Finally, the distance is set to $d = 71.48$ pc (Collaboration et al. 2020).

4 MODEL RESULTS AND DISCUSSION

While certainly not unique, our parametric model is fairly successful in reproducing the available data. The simulated images and the SED of the model are shown in Fig. 1 and Fig. 3 respectively.

The simulated image at 1.65 μm shows a similar radial structure to the one visible in the observations, displaying a two ringed disc, where Ring5 hides under the artificial coronagraph. The visible asymmetry in the SPHERE observations is reproduced using relatively large grains, $\sim 0.4 \mu\text{m}$, as smaller grains did not result in such strong forward scattering. As Stolker, T. et al. (2016) state, this forward scattering peak that is present in the observation may indicate that the dust grains in the disc surface are relatively large, suggesting that the disc is depleted of very-small grains. Interestingly, the model accurately shows the shadows described by D’Orazi et al. (2019) that are present in the SPHERE-IRDIS image.

The simulated 1.3 mm continuum image reproduces the two observed rings: the faint Ring13 and the brighter Ring24. The introduced Ring5 is not visible at the simulated image as its peak predicted intensities are around two times the noise in the ALMA image ($\sim 1 \times 10^{-7}$ Jy beam $^{-1}$). This gives us an upper limit for the total millimeter-sized dust mass present in Ring5 of $\sim 2 \times 10^{-5} M_\oplus$.

As the radial profiles obtained from the simulated images of the

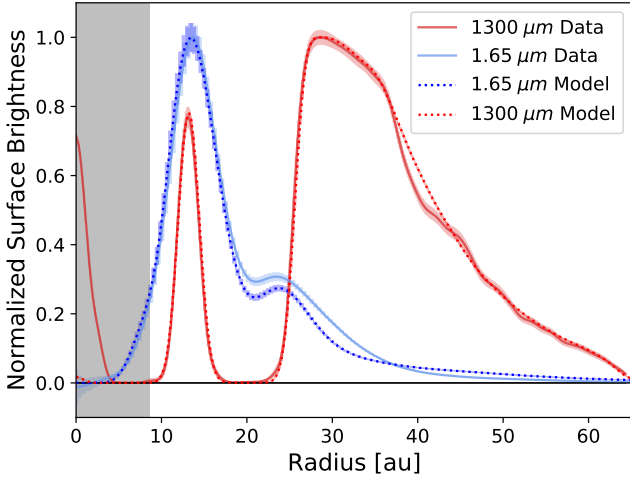


Figure 5. Comparison of the surface brightness profiles extracted from the deprojected synthetic images and observed H -band and 1.3 mm continuum images. The grey shaded area represents the radius of the artificial coronagraph used in the simulations (i.e., $\sim 0''.1$, or ~ 7.1 au at 71.48 pc).

model closely resemble those deduced from the observations (Fig. 5), we can assume that the model provides a possible approximation of the disc structure, including the dimensions of Ring13. Accordingly, taking the parametric model values for Ring13, it has a radius of 13.22 au, a FWHM of 2.00 au, and a scale height FWHM of the millimetre-size dust of 0.61 au. The total dust mass of Ring13 is about $0.7 M_{\oplus}$ in the model. In turn, our model reproduces the observations of Ring24 with peak intensity at ~ 30 au, and break at ~ 36 au. It contains a total dust mass of $\sim 44 M_{\oplus}$. The model predictions for the millimetre-size dust population in Ring13 are close to the measurements, with only a 0.07 au difference in the centroid location of the ring, and a 0.46 au difference in the width estimation. Since the scale height of the large grains in Ring13 is 0.61 au, and has a measured width of 2.46 au ***if you say measured you should give errors***, the ring is ~ 4.1 ***+-?*** times more extended radially than vertically.

The observed structure may point to the existence of planet-disc interactions within this system, where a giant planet depletes its orbit of gas and dust material. A possible constellation in this scenario is therefore the presence of two giant planets in the disc, one planet between the star and Ring13, and one planet between Ring13 and Ring24. As Ruíz-Rodríguez et al. (2019) suggest, the putative planet between Ring13 and Ring24 may be a giant planet with a mass within the range of 0.3 – $1.5 M_{\text{Jup}}$. This idea is supported by the similarity to the structure around HD 169142 which Bertrang et al. (2020) reproduced by including several giant planets.

The effective beam size of these new ALMA observations marginally resolves Ring13, with a width of $w_d = 2.46$ au. Using that the FWHM of Ring13 in the gas is $w_g = 5.42$ au from the RT model, we can see that large dust grains have to be radially converged. ***is w_d also a FWHM?***

Even though the radial spread of large dust grains in Ring13 appears to be quite thin, the width in comparison to the sub-lying gas profile speaks for the presence of considerable turbulent diffusion. Following a similar ring analysis as in Dullemond et al. (2018), we find that the ratio between the dimensionless diffusion parameter, D , and the dimensionless Stokes number, St , (which parameterizes the dynamical behaviour of a grain) is roughly, $D/St \approx 0.1$. The observed

signal is expected to be dominated by grains of size $a \approx 0.02$ cm. The RT model, together with the dust-to-gas ratio of 0.05, prescribe a gas density of $\Sigma_g \approx 0.5 \text{ g cm}^{-2}$ to the location of Ring13. With these values, the relevant Stokes number is approximated to be $St \approx 0.1$. This yields an estimate for the level of diffusivity of $D \approx 0.01$. It further provides a value for the level of turbulent viscosity in Ring13, $\alpha_{\text{turb}} \approx 0.01$, assuming viscosity to be equal to the level of diffusion (Youdin & Lithwick 2007). We note that an observation of molecular line broadening has found no evidence for turbulent contributions, suggesting $\alpha_{\text{turb}} < 0.01$ (Flaherty et al. 2020 *****REFERENCE*****). The value inferred from our model is just within this limit. It is linearly proportional to the local dust-to-gas ratio (by our definition of the gas surface density profile) – a standard ISM value of 0.01 for the dust-to-gas ratio would thus lead to an expected level of turbulent viscosity of $\alpha_{\text{turb}} \approx 5 \times 10^{-3}$. While the exact value for α_{turb} is not well constrained, the presence of turbulence is a robust detection, as it is required to explain the radial spread of the resolved Ring13.

The observed SED is compared with the model in Fig. 3. From the similarity with the data we propose that there has to be a small-grain population close to the stars down to 0.3 au. The observed central and compact signal in the ALMA observation cannot be explained using millimeter-sized dust, following the mass estimates in Section 2, as *****it reaches xxx times large surface densities than in the gas?***. Also, the hypothesis of thermal emission from large grain in the inner disk results in a large excess at $10 \mu\text{m}$ that does not match the data. The decision of employing the three ringed structure (i.e. add Ring5 to the observed structure) relies on the fact that the SED needed a ring at a radius around 5–7 au to have a proper fit around $10 \mu\text{m}$.

5 CONCLUSIONS

New ALMA 1.3 mm continuum imaging of the circumbinary disc around V4046 Sgr were analysed in the context of the available IR imaging and the observed spectral energy distribution using a RT model. The key conclusions are as follows.

(i) We report the detection of a narrow ring in the 1.3 mm continuum, with a radius 13.15 ± 0.26 au and an estimated width of 2.46 ± 0.56 au. The location of this ring is coincident with the inner ring observed in the scattered-light image, revealing that the ring includes around $0.7 M_{\oplus}$ millimetre-sized grains. Using the parametric model scale height value ($H = 0.60$ au at 13.15 au) we have that the ring width is roughly 4 times its estimated height.

(ii) The 1.3 mm outer ring, that starts at ~ 24 au and has its peak intensity at ~ 30 au, presents a visible break in the surface brightness at ~ 36 au.

(iii) We interpret the asymmetry observed with SPHERE-IRDIS at $1.65 \mu\text{m}$ as due to strong forward-scattering, which implies that the dust population is depleted of grains smaller than $\sim 0.4 \mu\text{m}$.

(iv) Our parametric model, which accounts for the SED of the system, involves the existence of a sub-micron dust population close (< 5 au) to the stars, and predicts the presence of another inner ring at ~ 5 au made mainly of small dust grains.

(v) The resolved radial width of Ring13 speaks for the presence of a considerable level of turbulent viscosity. ***SHOULD SAY HOW MUCH***

ACKNOWLEDGEMENTS

This paper makes use of the following ALMA data: ADS/JAO.ALMA #2017.0.01167.S. ALMA is a partnership of ESO (representing its member states), NSF (USA) and NINS (Japan), together with NRC (Canada), MOST and ASIAA (Taiwan), and KASI (Republic of Korea), in cooperation with the Republic of Chile. The Joint ALMA Observatory is operated by ESO, AUI/NRAO and NAOJ. The National Radio Astronomy Observatory is a facility of the National Science Foundation operated under cooperative agreement by Associated Universities, Inc.

This research has made use of the VizieR catalogue access tool, CDS, Strasbourg, France (DOI : 10.26093/cds/vizieR). The original description of the VizieR service was published in [Ochsenbein et al. \(2000\)](#).

This research has made use of the NASA/IPAC Infrared Science Archive, which is funded by the National Aeronautics and Space Administration and operated by the California Institute of Technology. S.C. acknowledges support from FONDECYT grant 1171624. S.P. acknowledges support from the Joint Committee of ESO and the Government of Chile and FONDECYT grant 1191934.

REFERENCES

- Andrews S. M., 2020, [ARA&A](#), **58**, 483
- Andrews S. M., Wilner D. J., Hughes A. M., Qi C., Dullemond C. P., 2009, [The Astrophysical Journal](#), **700**, 1502
- Andrews S. M., Wilner D. J., Hughes A. M., Qi C., Dullemond C. P., 2010, [The Astrophysical Journal](#), **723**, 1241
- Artymowicz P., Lubow S. H., 1994, [ApJ](#), **421**, 651
- Avenhaus H., et al., 2017, [The Astronomical Journal](#), **154**, 33
- Avenhaus H., et al., 2018, [The Astrophysical Journal](#), **863**, 44
- Bertrang G. H. M., Flock M., Keppler M., Trifonov T., Penzlin A. B. T., Avenhaus H., Henning T., Montesinos M., 2020, arXiv e-prints, [p. arXiv:2007.11565](#)
- Beuzit J. L., et al., 2019, [A&A](#), **631**, A155
- Cárcamo M., Román P. E., Casassus S., Moral V., Rannou F. R., 2018, [Astronomy and Computing](#), **22**, 16
- Casassus S., Cabrera G. F., Förster F., Pearson T. J., Readhead A. C. S., Dickinson C., 2006, [ApJ](#), **639**, 951
- Casassus S., et al., 2013, [Nature](#), **493**, 191
- Casassus S., et al., 2018, [MNRAS](#), **477**, 5104
- Casassus S., et al., 2019a, [MNRAS](#), **483**, 3278
- Casassus S., Pérez S., Osses A., Marino S., 2019b, [MNRAS](#), **486**, L58
- Castelli F., Gratton R. G., Kurucz R. L., 1997, [A&A](#), **318**, 841
- Collaboration G., Brown A. G. A., Vallenari A., Prusti T., de Bruijne J. H. J., Babusiaux C., Biermann M., 2020, Gaia Early Data Release 3: Summary of the contents and survey properties ([arXiv:2012.01533](#))
- Cutri R. M., et al. 2012, VizieR Online Data Catalog, [p. II/311](#)
- Cutri R. M., et al., 2003, VizieR Online Data Catalog, [p. II/246](#)
- D’Orazi V., et al., 2019, [Nature Astronomy](#), **3**, 167
- Donati J.-F., et al., 2011, [Monthly Notices of the Royal Astronomical Society](#), **417**, 1747
- Dullemond C. P., Juhasz A., Pohl A., Sereshti F., Shetty R., Peters T., Commercon B., Flock M., 2012, [The Astrophysical Journal](#)
- Dullemond C. P., et al., 2018, [ApJ](#), **869**, L46
- Garufi A., et al., 2020, [A&A](#), **633**, A82
- Helou G., Walker D. W., 1988, Infrared astronomical satellite (IRAS) catalogs and atlases. Volume 7, **7**
- Høg E., et al., 2000, [A&A](#), **355**, L27
- Hutchinson M. G., Evans A., Winkler H., Spencer Jones J., 1990, [A&A](#), **234**, 230
- Ishihara D., et al., 2010, [A&A](#), **514**, A1
- Jensen E. L. N., Mathieu R. D., 1997, [AJ](#), **114**, 301
- Kastner J. H., et al., 2018, [The Astrophysical Journal](#), **863**, 106
- Kharchenko N. V., 2001, [Kinematika i Fizika Nebesnykh Tel](#), **17**, 409
- Kurucz R. L., 1979, [ApJS](#), **40**, 1
- Mamajek E. E., Bell C. P. M., 2014, [Monthly Notices of the Royal Astronomical Society](#), **445**, 2169
- McJunkin M., France K., Schindhelm E., Herczeg G., Schneider P. C., Brown A., 2016, [ApJ](#), **828**, 69
- Murakami H., et al., 2007, [PASJ](#), **59**, S369
- Ochsenbein F., Bauer P., Marcout J., 2000, [A&AS](#), **143**, 23
- Ofek E. O., 2008, [PASP](#), **120**, 1128
- Pérez S., Casassus S., Baruteau C., Dong R., Hales A., Cieza L., 2019, [AJ](#), **158**, 15
- Qi C., et al., 2019, [ApJ](#), **882**, 160
- Quast G. R., Torres C. A. O., de La Reza R., da Silva L., Mayor M., 2000, IAU Symposium, **200**, 28
- Rodríguez D. R., Kastner J. H., Wilner D., Qi C., 2010, [The Astrophysical Journal](#), **720**, 1684
- Rosenfeld K. A., Andrews S. M., Wilner D. J., Stempels H. C., 2012, [The Astrophysical Journal](#), **759**, 119
- Rosenfeld K. A., Andrews S. M., Wilner D. J., Kastner J. H., McClure M. K., 2013, [The Astrophysical Journal](#), **775**, 136
- Ruíz-Rodríguez D., Kastner J. H., Dong R., Principe D. A., Andrews S. M., Wilner D. J., 2019, [The Astronomical Journal](#), **157**, 237
- Stolker, T. Dominik, C. Min, M. Garufi, A. Mulders, G. D. Avenhaus, H., 2016, [A&A](#), **596**, A70
- Youdin A. N., Lithwick Y., 2007, [Icarus](#), **192**, 588
- Zuckerman B., Song I., 2004, [Annual Review of Astronomy and Astrophysics](#), **42**, 685
- van Holstein R. G., et al., 2020, [A&A](#), **633**, A64

This paper has been typeset from a \LaTeX file prepared by the author.